

# TextureSplat: Per-Primitive Texture Mapping for Reflective Gaussian Splatting

MAE YOUNES, INRIA, France

ADNANE BOUKHAYMA, INRIA, France

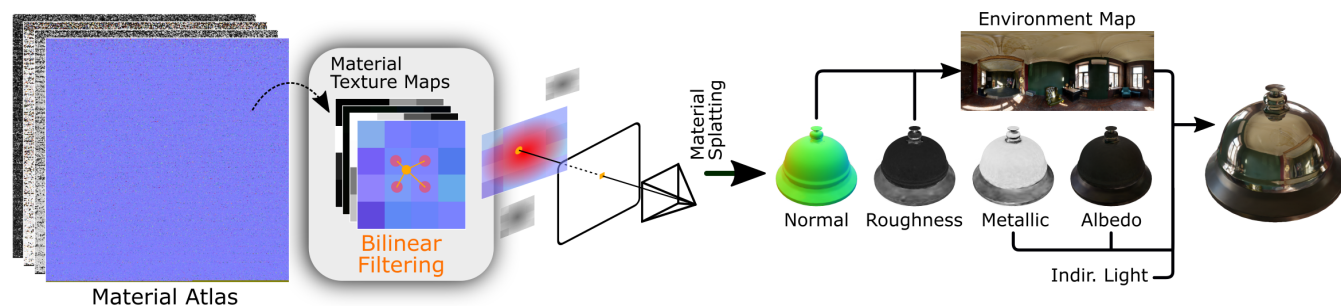


Fig. 1. *Method Overview*: We introduce planar primitive material textures — as opposed to single attributes — within physically based Gaussian Splatting rendering optimization. The increased representation power from spatially varying normal and material in object space enables fidelity reconstruction of high frequency specular in highly reflective scenes. Our hardware-accelerated implementation using texture atlases improves rendering efficiency at test time.

Gaussian Splatting have demonstrated remarkable novel view synthesis performance at high rendering frame rates. Optimization-based inverse rendering within complex capture scenarios remains however a challenging problem. A particular case is modelling complex surface light interactions for highly reflective scenes, which results in intricate high frequency specular radiance components. We hypothesize that such challenging settings can benefit from increased representation power. We hence propose a method that tackles this issue through a geometrically and physically grounded Gaussian Splatting borne radiance field, where normals and material properties are spatially variable in the primitive’s local space. Using per-primitive texture maps for this purpose, we also propose to harness the GPU hardware to accelerate rendering at test time via unified material texture atlas.

CCS Concepts: • **Computing methodologies** → **Rasterization; Rasterization; Point-based models; Texturing.**

## ACM Reference Format:

Mae Younes and Adnane Boukhayma. 2025. TextureSplat: Per-Primitive Texture Mapping for Reflective Gaussian Splatting. *ACM Trans. Graph.* 1, 1 (June 2025), 12 pages. <https://doi.org/10.1145/nnnnnnn.nnnnnnn>

## 1 INTRODUCTION

3D reconstruction and inverse rendering from multi-view images are pivotal problems receiving constant interest and investigation

from computer vision, graphics and machine learning research communities, with a myriad of direct applications in key industrial domains requiring high-quality 3D modeling and visualization.

Neural Radiance Fields (NeRF) [Mildenhall et al. 2020] revolutionized the field by representing scenes as continuous neural implicit functions optimized through differentiable volume rendering. Building on this foundation, 3D Gaussian Splatting (3DGS) [Kerbl et al. 2023] reintroduced point-based graphics by replacing neural networks with explicit 3D Gaussian primitives, achieving both real-time rendering and state-of-the-art quality. These primitives are rendered through volume resampling [Zwicker et al. 2002], with their parameters optimized via gradient descent-based differentiable rendering. More recently, 2D Gaussian Splatting (2DGS) [Huang et al. 2024] improved multi-view consistency by using planar Gaussian primitives that better align with surfaces.

Despite these advances, accurately representing highly reflective surfaces remains challenging. Reflective objects exhibit complex view-dependent effects that depend on surface normals, material properties, and environmental lighting. Recent methods such as RefGaussian [Yao et al. 2025] and 3DGS-DR [Ye et al. 2024] attempt to model these effects using per-Gaussian material properties and physically-based rendering approaches. However, they often struggle with high-frequency specular highlights and sharp reflections. We hypothesise that this is due in part to the inherent resolution limitations of using a single attribute value per primitive.

In this paper, we ask the question: *How can we enhance the representation power of Gaussian splatting for reflective scenes while maintaining computational efficiency and leveraging hardware acceleration?* Our key insight is that the planar nature of 2D Gaussian primitives naturally defines a parameterization that can be exploited for texture mapping, enabling us to store spatially varying material properties per primitive.

Inspired by the distinction between Gouraud shading [Gouraud 1971] (constant per-vertex attributes) and Phong shading [Phong

Authors’ addresses: Mae Younes, INRIA, France, [mae.younes.work@pm.me](mailto:mae.younes.work@pm.me); Adnane Boukhayma, INRIA, France, [adnane.boukhayma@inria.fr](mailto:adnane.boukhayma@inria.fr).

Permission to make digital or hard copies of all or part of this work for personal or classroom use is granted without fee provided that copies are not made or distributed for profit or commercial advantage and that copies bear this notice and the full citation on the first page. Copyrights for components of this work owned by others than ACM must be honored. Abstracting with credit is permitted. To copy otherwise, or republish, to post on servers or to redistribute to lists, requires prior specific permission and/or a fee. Request permissions from [permissions@acm.org](mailto:permissions@acm.org).

© 2025 Association for Computing Machinery.

0730-0301/2025/6-ART \$15.00

<https://doi.org/10.1145/nnnnnnn.nnnnnnn>

1975] (interpolated attributes) in traditional computer graphics, we introduce per-primitive texture maps for material properties in 2D Gaussian splatting. This approach effectively decouples the geometric representation (Gaussian primitives) from the appearance representation (material textures), allowing us to model high-frequency material variations without increasing the number of primitives.

Our method leverages the closed-form ray-splat intersection of 2DGS to accurately map screen-space pixels to local texture coordinates, enabling proper texture filtering. Crucially, we transform tangential normal maps to world space using the primitive's rotation matrix, analogous to normal mapping in traditional rendering. This enables detailed normal variations across each primitive's surface, significantly enhancing the rendering of specular highlights and reflections.

For efficient rendering after optimization, we pack the primitive textures into atlases that leverage GPU hardware-accelerated texture filtering operations. Our approach is fully compatible with deferred shading pipelines, allowing us to incorporate physically-based rendering models for accurate light interactions.

Through experiments on standard benchmarks for reflective scene reconstruction, we demonstrate that our method outperforms state-of-the-art approaches in terms of both quantitative metrics and visual quality. Our method achieves more accurate reflections and sharper specular highlights while maintaining real-time rendering performance. The benefits extend beyond reflective scenes, as our approach improves rendering quality for standard scenes as well.

Our contributions include:

- A per-primitive texture mapping approach for 2D Gaussian splatting that enhances representation power while maintaining computational efficiency.
- Leveraging a normal mapping technique in the context of Gaussian Splatting that significantly improves the quality of specular reflections.
- A hardware-accelerated implementation using texture atlases that enhances real-time rendering at test time.
- State-of-the-art results on benchmarks for reflective scene reconstruction, demonstrating significant improvements in rendering quality and accuracy.

## 2 RELATED WORK

Neural Radiance Fields [Mildenhall et al. 2020] (NeRFs) have been dominating the 3D shape and appearance modelling recently, based on the astounding success of implicit representations combined with differentiable volume rendering [Levoy 1988; Max 1995]. They represent scenes using view-dependent radiance and density fields parameterized by MLPs. When density is modeled as a function of a signed distance field, NeRF variants enable more accurate geometry reconstruction [Li et al. 2023; Wang et al. 2021; Wu et al. 2022; Yariv et al. 2021]. However, multi-scale volume rendering demands frequent MLP evaluations, limiting real-time performance. Grid-based methods [Chen et al. 2022; Fridovich-Keil et al. 2023, 2022; Müller et al. 2022; Sun et al. 2024, 2022] alleviate this but often struggle with large, unbounded scenes even with level-of-detail grids [Liu et al. 2020]. Gaussian splatting (3DGS) [Kerbl et al. 2023] emerged

lately as a strong alternative to NeRFs, offering state-of-the-art novel view synthesis and real time rendering frame rates. It extends the elliptical weighted average (EWA) volume resampling framework [Zwicker et al. 2001, 2002] to learnable [Kingma and Ba 2015] inverse rendering, modelling scenes with explicit Gaussian kernel primitives, that can be sorted and rasterized efficiently. The 2DGS representation [Huang et al. 2024] leverages planar 2D primitives instead of volumetric ones (3DGS), and performs precise 2D kernel evaluation in object space as opposed to approximative ones in screen space (3DGS), thus leading to superior geometric modelling and multi-view consistency.

Both vanilla NeRFs and 3DGS assume low-frequency view dependency. Hence, they can struggle with highly reflective scenes. One strategy to improve in this department is using shading functions that are reflection direction aware [Ge et al. 2023; Jiang et al. 2024b; Verbin et al. 2022]. For instance, Ref-NeRF [Verbin et al. 2022] extends NeRFs with a new parameterization for view-dependent radiance and incorporates normal vector regularization. The shading function can be more physically grounded, and this enables additional application such as relighting and material editing. In this regard, other NeRF and GS based methods proposed to model light interaction using the explicit rendering equation with BRDF functions. NeRV [Srinivasan et al. 2021] models reflectance and visibility fields separately for accurate relighting and editing. NeRO [Liu et al. 2023] Learns surface normals and view-dependent radiance jointly using RGB and environment maps. EnviDR [Liang et al. 2023] Uses environment maps to capture spatially-varying reflections in neural rendering. The next wave of work tackled shading for Gaussian Splatting (e.g. [Gao et al. 2024; Jiang et al. 2024a; Liang et al. 2024; Tang and Cham 2024; Yao et al. 2025; Ye et al. 2024; Zhu et al. 2024]). GShader [Jiang et al. 2024a] applies a simplified shading function on each fragment. 3DGS-DR [Ye et al. 2024] introduces deferred shading at pixel level, and stabilizes the optimization by smoothing out normal gradients. 3iGS [Tang and Cham 2024] introduces tensor decomposition of spherical harmonics. GS-ROR [Zhu et al. 2024] uses signed distance function priors to improve specular rendering. [Gao et al. 2024] employs ray-tracing to model inter-reflections. It approximates the rendering equation with Monte Carlo sampling which reduces rendering speed. Building on the 2DGS representation, our baseline Ref-Gaussian [Yao et al. 2025] decomposes the scene into geometry, material and lighting through the split-sum approximation of the rendering equation while incorporating an indirect light attribute, enabling inter-reflections while being fast to render. It achieves the state-of-the-art performance on the standard reflective scene novel view synthesis benchmarks. We propose to improve of its physical material and normal representations.

In parallel with our work, we noticed that a few papers [Chao et al. 2025; Huang and Gong 2024; Xu et al. 2024] introduce the texture attribute representation for Gaussian Splatting as well. They use it to model a view independent component of the color. Differently, we explore this representation for rendering material properties and normals within 2DGS enabled physically based rendering to reconstruct challenging highly reflective scenes. Differently, we also propose leveraging texture atlases to enable hardware acceleration at test-time rendering.

### 3 METHOD

In this section, we present our approach to enhance 2D Gaussian Splatting (2DGS) [Huang et al. 2024] for representing highly reflective 3D scenes. We first provide background on 2DGS, then introduce our per-primitive texture mapping method that enables high-frequency detail on flat Gaussian primitives. Finally, we describe our hardware-accelerated implementation using texture atlases and the physically-based rendering model we use for reflective scenes.

#### 3.1 Background: 2D Gaussian Splatting

We build upon 2D Gaussian Splatting (2DGS) [Huang et al. 2024], which represents a scene using oriented planar disks offering improved multi-view consistency compared to 3D Gaussian Splatting [Kerbl et al. 2023]. Each primitive  $k$  is characterized by its position  $\mathbf{p}_k$ , tangential vectors  $\mathbf{t}_{u_k}$  and  $\mathbf{t}_{v_k}$ , and scaling factors  $(s_{u_k}, s_{v_k})$ . The primitive's normal is defined by the cross product  $\mathbf{n}_k = \mathbf{t}_{u_k} \times \mathbf{t}_{v_k}$ .

The 2D Gaussian is defined in a local tangent plane in world space with coordinates  $(u, v)$ , parameterized as:

$$P_k(u, v) = \mathbf{p}_k + s_{u_k} \mathbf{t}_{u_k} u + s_{v_k} \mathbf{t}_{v_k} v = \mathbf{H}_k(u, v, 1, 1)^T, \quad (1)$$

$$\text{where } \mathbf{H}_k = \begin{bmatrix} s_{u_k} \mathbf{t}_{u_k} & s_{v_k} \mathbf{t}_{v_k} & \mathbf{0} & \mathbf{p}_k \\ 0 & 0 & 0 & 1 \end{bmatrix} \in \mathbb{R}^{4 \times 4}. \quad (2)$$

For a point  $(u, v)$  in the local coordinate space, the 2D Gaussian value is evaluated as:

$$\mathcal{G}_k(u, v) = \exp\left(-\frac{u^2 + v^2}{2}\right). \quad (3)$$

Given pixel  $(x, y)$ , Gaussians are rendered through ray-primitive plane intersection  $(u, v)$  computation [Zwicker et al. 2004]:

$$\mathbf{x}_{ray} = (xz, yz, z, 1)^T = \mathbf{W} \mathbf{H}_k(u, v, 1, 1)^T, \quad (4)$$

where  $\mathbf{W}$  is the view transformation matrix. The intersection is computed efficiently by transforming two orthogonal planes defined by the ray into the splat's local coordinate system:

$$\mathbf{h}_{u,k} = (\mathbf{W} \mathbf{H}_k)^T (-1, 0, 0, x)^T, \quad \mathbf{h}_{v,k} = (\mathbf{W} \mathbf{H}_k)^T (0, -1, 0, y)^T. \quad (5)$$

This yields a closed-form solution for the intersection coordinates:

$$u_k(x, y) = \frac{\mathbf{h}_{u,k}^2 \mathbf{h}_{v,k}^4 - \mathbf{h}_{u,k}^4 \mathbf{h}_{v,k}^2}{\mathbf{h}_{u,k}^1 \mathbf{h}_{v,k}^2 - \mathbf{h}_{u,k}^2 \mathbf{h}_{v,k}^1}, \quad v_k(x, y) = \frac{\mathbf{h}_{u,k}^4 \mathbf{h}_{v,k}^1 - \mathbf{h}_{u,k}^1 \mathbf{h}_{v,k}^4}{\mathbf{h}_{u,k}^1 \mathbf{h}_{v,k}^2 - \mathbf{h}_{u,k}^2 \mathbf{h}_{v,k}^1}, \quad (6)$$

where  $\mathbf{h}^i$  denotes the  $i$ -th component of the vector.

Each splat has also a learnable opacity  $\alpha_k$ . The final pixel color is computed by alpha-blending all primitives that contribute to the pixel in front-to-back order:

$$\mathbf{A}(x, y) = \sum_{i=1}^N \mathbf{a}_i \alpha_i(x, y) \prod_{j=1}^{i-1} (1 - \alpha_j(x, y)) \quad (7)$$

where  $\alpha_i(x, y) = \alpha_i \mathcal{G}_i(u_i(x, y), v_i(x, y))$  is the effective opacity of the  $i$ -th primitive at pixel  $(x, y)$  and  $\mathbf{a}_i$  is its attribute (e.g., color), typically represented using spherical harmonics for view-dependent effects.

#### 3.2 Per-Primitive Texture Mapping

While existing Gaussian splatting methods assign a single attribute value per primitive, we observe that the flat nature of 2D Gaussians naturally defines a local parameterization that can be leveraged for texture mapping. This enables encoding higher-frequency spatial detail without increasing the number of primitives, analogous to the distinction between Gouraud shading (constant per-primitive attributes) and Phong shading (interpolated attributes) in traditional rendering.

Rather than representing material properties with a single value per primitive, we define them as texture maps in the splat's local coordinate system:

$$\mathbf{a}_k(x, y) = \mathcal{T}_k(u_k(x, y), v_k(x, y)) \quad (8)$$

where  $\mathcal{T}_k$  is the texture map associated with the  $k$ -th primitive, and  $\mathbf{a}_k$  represents any reconstructed attribute.

The original Elliptical Weighted Average (EWA) splatting paper [Zwicker et al. 2002] assumed constant attributes within the projected kernel's footprint for analytical screen-space filtering, a characteristic inherited by standard 3DGS [Kerbl et al. 2023]. However, the 2DGS formulation we adopt [Huang et al. 2024] computes ray-splat intersections directly and does not rely on EWA-style screen-space filtering, making it naturally suited for spatially varying attributes defined on the splat itself.

This approach provides several advantages:

**Decoupling of geometry and appearance:** By separating the geometric representation (Gaussian primitives) from the appearance details (textures), we can represent complex visual features without increasing the number of primitives.

**Memory efficiency:** Fewer primitives means reduced memory usage, improved cache coherence, faster rasterization and sorting operations.

**Higher fidelity appearance:** Textures can capture high-frequency detail that would otherwise require many more primitives to represent.

**Normal mapping:** Instead of using a single normal per primitive, we can store detailed normal maps, significantly improving the rendering of specular effects.

The 2DGS representation is particularly well-suited for texture mapping because the ray-splat intersection already provides exact  $(u, v)$  coordinates in the primitive's local space and thus, enables accurate texture filtering.

#### 3.3 Texture Mapping Implementation

To implement our texture mapping approach, we map the local splat coordinates  $(u, v)$  to texture coordinates  $(s, t)$  that account for the Gaussian kernel's support. Since the Gaussian kernel effectively drops to zero at approximately  $S_\sigma = 3$  standard deviations, we scale the local coordinates to ensure that the effective support of the Gaussian  $([-S_\sigma, S_\sigma] \times [-S_\sigma, S_\sigma])$  maps to the texture space  $[0, 1] \times [0, 1]$ :

$$s = \frac{u + S_\sigma}{2S_\sigma}, \quad t = \frac{v + S_\sigma}{2S_\sigma}. \quad (9)$$

The attribute value  $\mathbf{a}_k(x, y)$  for primitive  $k$  at pixel  $(x, y)$  is then obtained by bilinear filtering from its texture map  $\mathcal{T}_k$ :

$$\mathbf{a}_k(x, y) = \text{BilinearFilter}(\mathcal{T}_k, s(u_k(x, y)), t(v_k(x, y))). \quad (10)$$

### 3.4 Hardware Acceleration via Texture Atlases

To efficiently render optimized scenes at test time with per-primitive textures, we leverage hardware-accelerated texture filtering by packing individual primitive textures into texture atlases. This approach is inspired by methods like Ptex [Burley and Lacewell 2008] and seamless texture atlases [Purnomo et al. 2004], adapted to the specific needs of Gaussian splatting.

**3.4.1 Texture Atlas Construction.** Each splat is associated with a small, fixed-resolution texture (e.g.,  $T \times T$  texels, where  $T$  is typically 4, 8, or 16). For  $P$  splats and  $C$  total channels for all textured attributes, this  $P \times C \times T \times T$  texel data is organized into one or more large 2D atlas textures. We pack the individual primitive textures into larger texture atlases that can be efficiently accessed by the GPU by determining the maximum atlas dimensions based on GPU capabilities, calculating how many  $T \times T$  textures fit along each dimension, computing the total number of textures per atlas, then determining the number of atlases needed.

To efficiently access the textures within the atlas, we create an indirection buffer that maps primitive IDs to texture chart coordinates within the atlas. This buffer stores the top-left corner coordinates ( $\text{chart\_idx\_x}, \text{chart\_idx\_y}$ ) of each primitive's texture in the atlas. Since CUDA texture objects typically support up to 4 channels, multiple atlases are used if the total number of attribute channels exceeds this (e.g., one atlas for albedo (RGB) and roughness (A), another for tangent normals (RGB) and metallic (A)).

**3.4.2 Accelerated Texture Sampling.** During test-time rendering, we perform texture sampling using hardware-accelerated filtering:

- (1) For a given primitive  $k$  and local coordinates  $(u, v)$ , we map to normalized texture coordinates  $(s, t) \in [0, 1] \times [0, 1]$  as described above.
- (2) We retrieve the chart coordinates ( $\text{chart\_idx\_x}, \text{chart\_idx\_y}$ ) from the indirection buffer.
- (3) We compute the atlas coordinates:

$$s_{\text{atlas}} = \frac{\text{chart\_idx\_x} \cdot T + s \cdot T}{N_{\text{charts}_x} \cdot T}, \quad t_{\text{atlas}} = \frac{\text{chart\_idx\_y} \cdot T + t \cdot T}{N_{\text{charts}_y} \cdot T}, \quad (11)$$

where  $N_{\text{charts}_x}$  and  $N_{\text{charts}_y}$  are the total number of charts along the width and height of the atlas, respectively.

- (4) We sample the atlas using hardware-accelerated bilinear filtering with CUDA's 'tex2D()' intrinsic:

$$\mathbf{a}_k(x, y) = \text{BilinearFilter}(\text{atlas}, s_{\text{atlas}}, t_{\text{atlas}}). \quad (12)$$

This approach fully leverages the GPU's texture units for filtering, which are significantly faster than software-based sampling approaches. It leverages dedicated texture caching and filtering hardware, significantly speeding up attribute fetching compared to manual interpolation from global memory arrays. By using texture atlases, we avoid the need for multiple texture bindings during rendering, improving performance and reducing API overhead.

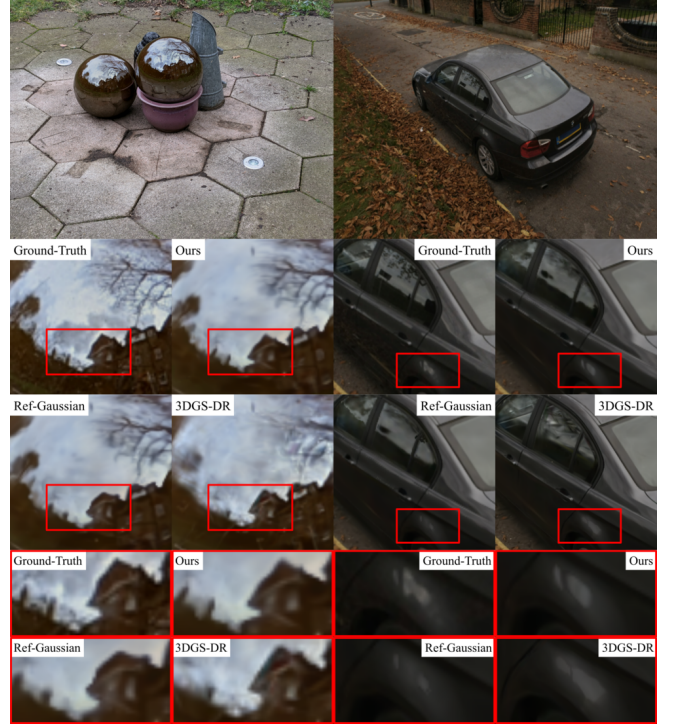


Fig. 2. Qualitative comparisons of novel view synthesis on real scenes. From left to right: garden spheres and sedan.

### 3.5 Physically-Based Deferred Rendering

Following the deferred rendering approach used in 3DGS-DR [Ye et al. 2024] and Ref-Gaussian [Yao et al. 2025], we first splat material attributes to screen-space buffers, then apply physically-based shading in a separate pass.

**3.5.1 Material Properties.** Each 2D Gaussian is associated with texture maps for the following material properties: Albedo  $\lambda \in [0, 1]^3$ , Metallic  $m \in [0, 1]$ , Roughness  $r \in [0, 1]$ , Tangent normal  $\mathbf{n}^t \in [0, 1]^3$ . Represents normal perturbations in the tangent space. For memory efficiency, we encode tangent normals using only two components ( $n_x^t, n_y^t$ ) and reconstruct the third component at runtime using  $n_z^t = \sqrt{\max(0, 1 - (n_x^t)^2 - (n_y^t)^2)}$ .

**3.5.2 Normal Mapping.** A key factor in our approach is the use of normal mapping instead of a single normal per primitive. The tangent normal map encodes normal perturbations in the primitive's local coordinate system. These are transformed to world space using:

$$\mathbf{n}_k(x, y) = \mathbf{R}_k \cdot \mathbf{n}_k^t(x, y) = [\mathbf{t}_{u_k}, \mathbf{t}_{v_k}, \mathbf{t}_{u_k} \times \mathbf{t}_{v_k}] \cdot \mathbf{n}_k^t(x, y), \quad (13)$$

where  $\mathbf{R}_k$  is the primitive's rotation matrix. This enables detailed normal variations across the surface of each primitive, critical for capturing high-frequency specular effects.



Table 1. Per-scene image quality comparison in the reflective novel view synthesis setting.

Datasets		Shiny Blender [Verbin et al. 2022]						Glossy Synthetic [Liu et al. 2023]								Real [Verbin et al. 2022]		
		ball	car	coffee	helmet	teapot	toaster	angel	bell	cat	horse	luyu	potion	tbell	teapot	garden	sedan	toycar
PSNR ↑	Ref-NeRF	33.16	30.44	33.99	29.94	45.12	26.12	20.89	30.02	29.76	19.30	25.42	30.11	26.91	22.77	22.01	25.21	23.65
	ENVIDR	41.02	27.81	30.57	32.71	42.62	26.03	29.02	30.88	31.04	25.99	28.03	32.11	28.64	26.77	21.47	24.61	22.92
	3DGS	27.65	27.26	32.30	28.22	45.71	20.99	24.49	25.11	31.36	24.63	26.97	30.16	23.88	21.51	21.75	26.03	23.78
	2DGS	25.97	26.38	32.31	27.42	44.97	20.42	26.95	24.79	30.65	25.18	26.89	29.50	23.28	21.29	22.53	26.23	23.70
	GShader	30.99	27.96	32.39	28.32	45.86	26.28	25.08	28.07	31.81	26.56	27.18	30.09	24.48	23.58	21.74	24.89	23.76
	3DGS-DR	33.43	30.48	34.53	31.44	47.04	26.76	29.07	30.60	32.59	26.17	28.96	32.65	29.03	25.77	21.82	26.32	23.83
	Ref-Gaussian	36.07	31.32	34.2	32.3	47.15	28.28	30.55	28.57	33.04	26.76	30.1	33.39	30.1	25.97	23.09	26.23	24.74
	Ours	39.06	31.72	34.85	33.16	48.25	28.59	30.95	28.94	33.56	27.26	30.55	34.12	30.74	26.81	23.27	26.5	24.83
SSIM ↑	Ref-NeRF	0.971	0.950	0.972	0.954	0.995	0.921	0.853	0.941	0.944	0.820	0.901	0.933	0.947	0.897	0.584	0.720	0.633
	ENVIDR	0.997	0.943	0.962	0.987	0.995	0.922	0.934	0.954	0.965	0.925	0.931	0.960	0.947	0.957	0.561	0.707	0.549
	3DGS	0.937	0.931	0.972	0.951	0.996	0.894	0.792	0.908	0.959	0.797	0.916	0.938	0.900	0.881	0.571	0.771	0.637
	2DGS	0.934	0.930	0.972	0.953	0.997	0.892	0.918	0.911	0.958	0.909	0.918	0.939	0.902	0.886	0.609	0.778	0.597
	GShader	0.966	0.932	0.971	0.951	0.996	0.929	0.914	0.919	0.961	0.933	0.914	0.936	0.898	0.901	0.576	0.728	0.637
	3DGS-DR	0.979	0.963	0.976	0.971	0.997	0.942	0.942	0.959	0.973	0.933	0.943	0.959	0.958	0.942	0.581	0.773	0.639
	Ref-Gaussian	0.985	0.966	0.976	0.971	0.997	0.952	0.956	0.943	0.975	0.942	0.953	0.966	0.947	0.942	0.628	0.766	0.679
	Ours	0.991	0.969	0.977	0.976	0.998	0.954	0.959	0.946	0.977	0.947	0.957	0.971	0.97	0.951	0.626	0.77	0.68
LPIPS ↓	Ref-NeRF	0.166	0.050	0.082	0.086	0.012	0.083	0.144	0.102	0.104	0.155	0.098	0.084	0.114	0.098	0.251	0.234	0.231
	ENVIDR	0.020	0.046	0.083	0.036	0.009	0.081	0.067	0.054	0.049	0.065	0.059	0.072	0.069	0.041	0.263	0.387	0.345
	3DGS	0.162	0.047	0.079	0.081	0.008	0.125	0.088	0.104	0.062	0.077	0.064	0.093	0.102	0.125	0.248	0.206	0.237
	2DGS	0.156	0.052	0.079	0.079	0.008	0.127	0.072	0.109	0.060	0.071	0.066	0.097	0.125	0.101	0.254	0.225	0.396
	GShader	0.121	0.044	0.078	0.074	0.007	0.079	0.082	0.098	0.056	0.562	0.064	0.088	0.091	0.122	0.274	0.259	0.239
	3DGS-DR	0.105	0.033	0.076	0.050	0.006	0.082	0.052	0.050	0.042	0.057	0.048	0.068	0.059	0.060	0.247	0.208	0.231
	Ref-Gaussian	0.089	0.031	0.078	0.048	0.006	0.067	0.040	0.067	0.037	0.049	0.043	0.061	0.070	0.059	0.266	0.258	0.257
	Ours	0.075	0.027	0.075	0.039	0.004	0.066	0.037	0.065	0.034	0.043	0.040	0.052	0.041	0.051	0.276	0.250	0.263

**3.5.3 Attribute Splatting.** We splat the material attributes to screen-space buffers using alpha-blending:

$$X(x, y) = \sum_{i=1}^N \mathbf{x}_i(x, y) \alpha_i(x, y) \prod_{j=1}^{i-1} (1 - \alpha_j(x, y)), \quad (14)$$

where  $X$  represents the combined screen-space buffers:

$$X = \begin{bmatrix} \Lambda \\ M \\ R \\ \mathbf{N} \\ L_{\text{ind}} \end{bmatrix}, \quad \mathbf{x}_i = \begin{bmatrix} \lambda_i(x, y) \\ m_i(x, y) \\ r_i(x, y) \\ \mathbf{n}_i(x, y) \\ l_i^{\text{ind}}(x, y) \end{bmatrix} \quad (15)$$

This deferred approach treats alpha-blending as a smoothing filter, stabilizing the optimization of features sampled from textures and producing more cohesive rendering results compared to shading directly on the Gaussians [Yao et al. 2025; Ye et al. 2024].

**3.5.4 Physically-Based Shading.** With the aggregated material maps, we apply the rendering equation to compute the outgoing radiance  $L_o(x, y, \omega_o)$  in the direction  $\omega_o$ :

$$L_o(x, y, \omega_o) = L_d(x, y, \omega_o) + L_s(x, y, \omega_o). \quad (16)$$

The diffuse term writes:

$$L_d(x, y, \omega_o) = \frac{\Lambda(x, y)}{\pi} (1 - M(x, y)) \mathcal{L}_{\text{env}}^{\text{diffuse}}(\mathbf{N}(x, y)), \quad (17)$$

where  $\mathcal{L}_{\text{env}}^{\text{diffuse}}$  is the pre-integrated diffuse environment irradiance. Following the split-sum approximation, we compute the specular component efficiently:

$$L_s(x, y, \omega_o) \approx \text{BRDF}_{LUT}(\mathbf{N}(x, y) \cdot \omega_o, R(x, y)) \cdot (V(x, y) L_{\text{dir}}(x, y, \omega_r, R(x, y)) + (1 - V(x, y)) L_{\text{ind}}(x, y)). \quad (18)$$

The first term,  $\text{BRDF}_{LUT}$ , depends solely on the view angle and roughness, which we precompute and store in a 2D lookup texture.  $L_{\text{dir}}(x, y, \omega_r, R(x, y))$  is the direct environment lighting queried from a learnable environment map in the reflection direction  $\omega_r = \text{reflect}(-\omega_o, \mathbf{N}(x, y))$ , using roughness  $R(x, y)$  for mipmap selection.  $L_{\text{ind}}(x, y)$  is the blended indirect lighting component.

**3.5.5 Inter-reflection Modeling.** To handle inter-reflections, we separately model direct light  $L_{\text{dir}}$  (not blocked by scene elements) and indirect light  $L_{\text{ind}}$  (all other light). We approximate the visibility  $V(x, y) \in \{0, 1\}$  of incident light by ray-tracing an extracted mesh as in [Yao et al. 2025] to determine whether light is self-occluded along the reflected direction. For the indirect lighting component, each Gaussian is assigned an additional view-dependent color  $l_k^{\text{ind}}$ , modeled by spherical harmonics. During rendering,  $l_k^{\text{ind}}$  is evaluated in the reflected direction at the Gaussian level, and alpha blending is applied to aggregate the indirect lighting map.

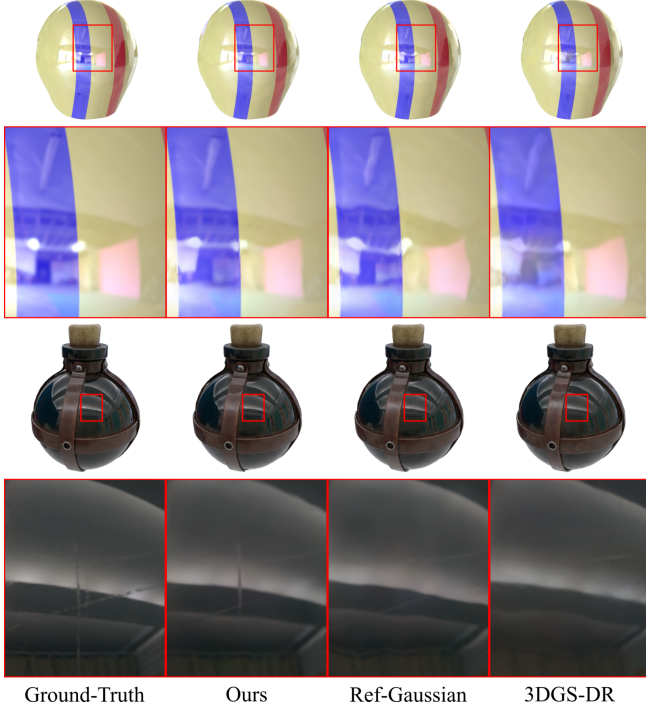


Fig. 3. Qualitative comparisons of novel view synthesis on synthetic scenes. From top to bottom: helmet and potion.

### 3.6 Training

Splat parameters  $\mathbf{p}_k, \mathbf{t}_{u_k}, \mathbf{t}_{v_k}, \mathbf{s}_{u_k}, \mathbf{s}_{v_k}, \mathbf{o}_k$ , their material texture maps  $\mathcal{T}_k^\lambda, \mathcal{T}_k^m, \mathcal{T}_k^r, \mathcal{T}_k^{n^i}$ , per-splat indirect lighting SH coefficients for  $\mathbf{l}_k^{\text{ind}}$ , and the environment maps ( $\mathcal{L}_{\text{env}}^{\text{diffuse}}, \mathcal{L}_{\text{env}}^{\text{spec}}$ ), are optimized end-to-end using a composite loss:

$$\mathcal{L} = \mathcal{L}_{\text{img}} + \lambda_n \mathcal{L}_n + \lambda_{\text{smooth}} \mathcal{L}_{\text{smooth}}, \quad (19)$$

where  $\mathcal{L}_{\text{img}} = (1 - \lambda) \mathcal{L}_1 + \lambda \mathcal{L}_{\text{D-SSIM}}$  is the RGB reconstruction loss with balancing weight  $\lambda = 0.2$ . The normal consistency loss  $\mathcal{L}_n = 1 - \tilde{\mathbf{N}}(x, y)^T \mathbf{N}(x, y)$  encourages alignment of the Gaussians with the surface by minimizing the cosine difference between the rendered normal  $\mathbf{N}(x, y)$  and the surface normal  $\tilde{\mathbf{N}}(x, y)$  derived from rendered depth. The edge-aware normal smoothness loss  $\mathcal{L}_{\text{smooth}} = \|\nabla \mathbf{N}(x, y)\| \exp(-\|\nabla C_{gt}(x, y)\|)$  regularizes normal variation in regions of low texture, where  $C_{gt}$  is the ground truth image. During training, we periodically extract the object's surface mesh using truncated signed distance function (TSDF) fusion to compute ray-surface intersections for visibility checks, accelerated using a bounding volume hierarchy (BVH). We use a single NVIDIA RTX A6000 GPU for our evaluations.

## 4 EXPERIMENTS

Following our baseline method [Yao et al. 2025], we evaluate our work quantitatively and qualitatively under standard multi-view reconstruction benchmarks of challenging reflective scenes. We use

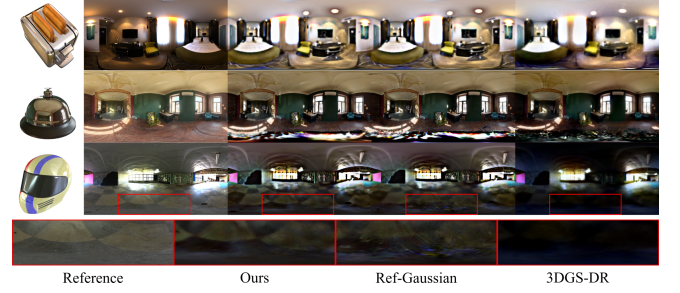


Fig. 4. Qualitative comparisons of environment maps estimated by different methods.

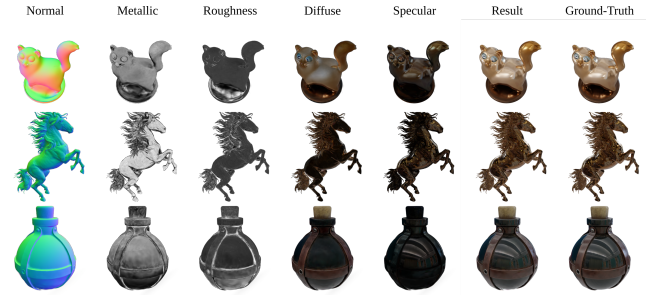


Fig. 5. Decomposition results of our method. From top to bottom: cat, horse and potion.

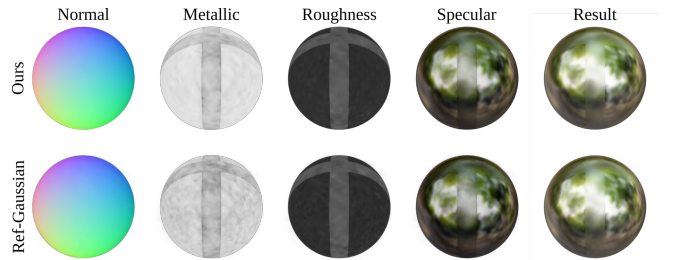


Fig. 6. Comparison of scene decomposition between our method and the baseline.

Table 2. Normal quality evaluated by MAE<sup>°</sup>: comparisons on the Shiny Blender Dataset.

	GShader	NVDiffRec	ENVIDR	3DGS-DR	Ref-Gaussian	Ours
MAE <sup>°</sup> ↓	22.31	17.02	4.618	4.871	2.078	1.83

the datasets: Shiny Blender [Verbin et al. 2022] and Glossy Synthetic [Liu et al. 2023] for novel view synthesis of reflective objects, and dataset Ref-Real [Verbin et al. 2022] to account for real world open reflective scenes. We also provide results on the Synthetic NeRF [Mildenhall et al. 2020] dataset to showcase our method under non-reflective scenes and illustrate its practicality. We compare to state-of-the-art methods in the reflective scene setting, including method Ref-Gaussian [Yao et al. 2025], with whom we share the

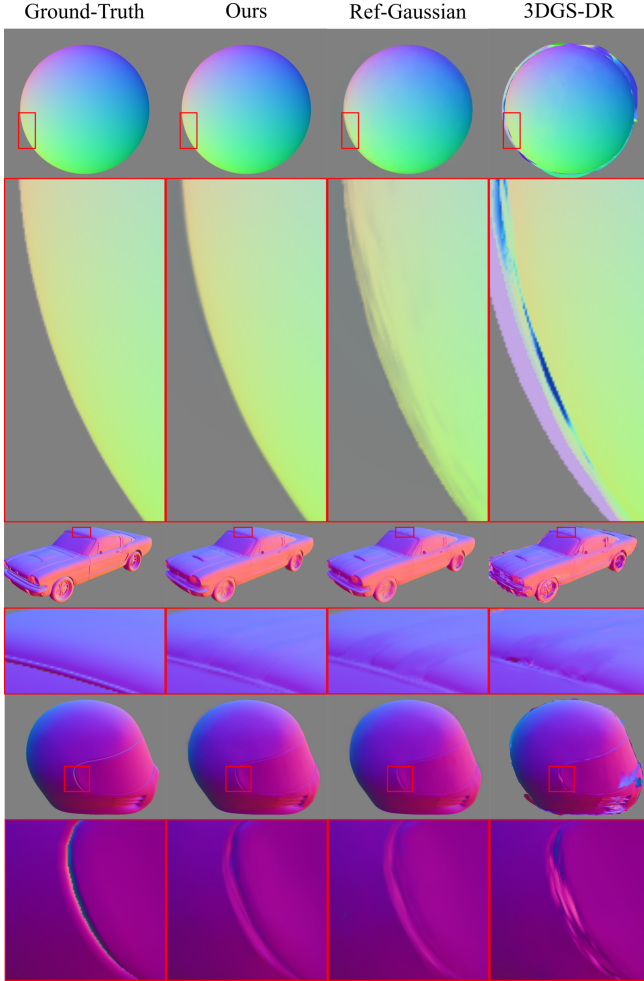


Fig. 7. Qualitative comparisons of normal rendering by different methods

same underlying physics based model and training strategy, competitive reflective Gaussian splatting based methods GShader [Jiang et al. 2024a] and 3DGS-DR [Ye et al. 2024], 3DGS [Kerbl et al. 2023] and 2DGS [Huang et al. 2024] for reference, and seminal NeRF based approaches such as Ref-NeRF [Verbin et al. 2022] and EN-VIDR [Liang et al. 2023]. We provide additional results and ablation studies in the supplementary material.

#### 4.1 Implementation Details

For a stable optimization, we follow a two-stage optimization approach, where we first train for half the total number of iterations using per-splat single attribute optimization. During the second stage, we start optimizing the material and normal textures initialized from the corresponding attributes from the first stage and we freeze the positions of the primitives.

In all our evaluations, we use texture resolution of  $4 \times 4$ .

We use the same hyper-parameters and training strategies defined by Ref-Gaussian [Yao et al. 2025] as we build on it and consider it our main baseline method.

We also follow Ref-Gaussian [Yao et al. 2025] in replacing the integrated diffuse lighting by a spherical harmonics view dependent color for better fitting in the reflective setting.

We implement efficient CUDA kernels on top of 2DGS and Ref-Gaussian for forward and backward operations involving material textures and normal mapping, as well as the texture atlases construction, packing and hardware bilinear filtering at test time.

#### 4.2 Novel View Synthesis

Table 1 shows numerical results in the standard reflective benchmark. We report Peak Signal-to-Noise Ratio (PSNR), Structural Similarity Index Measure (SSIM) [Wang et al. 2004], and Learned Perceptual Image Patch Similarity (LPIPS) [Zhang et al. 2018] as metrics. Our method outperforms the competition, including baseline Ref-Gaussian, which is also the state-of-the-art method currently under this benchmark to the best of our knowledge. We provide qualitative results to accompany this table, for real scenes in Figure 2 and synthetic ones in Figure 3. Our method displays superior ability in capturing reflections on the surface with more fidelity, while competition Ref-Gaussian and 3DGS-DR suffer from distorted or missing reflections. We also show in the supplementary material numerical and qualitative comparisons under non-reflective data on Nerf Synthetic Scenes [Mildenhall et al. 2020]. Here our method performs competitively with the competition. The improvement brought by our method over the baseline Ref-Gaussian particularly, under both reflective and non-reflective scenes, is a testimony of the efficacy and versatility of our representation.

#### 4.3 Scene Decomposition

Despite the under-constrained nature of the task in many cases, our optimization yields stable and physically plausible scene property factorization. Figure 5 illustrates decomposition examples for reflective objects into geometry normals, roughness and metallic. We also show the diffuse and specular components, in addition to the final rendering which preserves the groundtruth. The specular highlights are mostly successfully factored out from the view-independent component. Figure 6 shows a comparison of the decomposition with respect to our baseline method. Notice that our material properties are sharper and display less noise. Our normals replicate the smooth sphere shape more faithfully. We compare estimated environment maps for our method and the competition in Figure 4. Notice that our estimated scene lighting bares more similarity with the reference maps and display less distortions and artefacts generally, compared to our baseline.

We evaluate our normal estimation through the benchmark of the Shiny Blender dataset [Verbin et al. 2022]. Table 2 reports the mean angular error of normal maps, where we outperform our baseline and the competition. This results validates our tangential normal representation and the use of normal mapping, as also confirmed by our superior qualitative results (Figure 7).

#### 4.4 Hardware Acceleration Performance

While our per-primitive texture mapping approach improves rendering quality for reflective scenes, a potential concern is the additional



Table 3. Rendering performance comparison between software bilinear filtering and hardware-accelerated texture atlas filtering at different texture resolutions. Values represent the ratio of FPS compared to the baseline method without textures, averaged across the Shiny Blender dataset scenes.

	4×4 Textures	8×8 Textures	16×16 Textures
Baseline (No Textures)	1.00×	1.00×	1.00×
Software Bilinear	0.95×	0.96×	0.85×
Hardware Texture Atlas	0.96×	0.97×	0.93×

computational cost of texture sampling. To address this, we implemented hardware-accelerated texture filtering using texture atlases as described in Section 3.4. In this section, we evaluate the performance benefits of this implementation compared to software-based bilinear filtering.

We trained our model on the Shiny Blender dataset using three different texture resolutions: 4×4, 8×8, and 16×16. For each model, we then rendered the scenes using both the software implementation of bilinear filtering and our hardware-accelerated implementation with texture atlases. We measured the rendering performance in frames per second (FPS) and compared these values to the baseline method without textures.

As shown in Table 3, software-based bilinear filtering introduces some performance overhead compared to the baseline. This overhead increases with higher texture resolutions.

In contrast, our hardware-accelerated implementation with texture atlases maintains rendering performance very close to the baseline method in comparison. The performance remains strong even at higher texture resolutions.

These results demonstrate that the texture atlas approach effectively leverages GPU hardware capabilities to minimize the performance impact of texture filtering. Several factors contribute to this efficiency including the use of dedicated texture units that are designed specifically for texture filtering operations, and are substantially faster than general-purpose compute. The gap can be widened even more when applied to more complicated objects or larger scenes.

We note that there is still room for improvement as we do not follow any strategy for packing the texture into the atlases, which could benefit from better locality if considering only primitives that are used for each frame or packing textures belonging to nearby primitives next to each other.

By leveraging hardware acceleration through texture atlases, we can achieve the best of both worlds: the improved rendering quality of per-primitive textures for reflective scenes while maintaining rendering performance comparable to methods without textures.

#### 4.5 Ablation Study

To evaluate the effectiveness of our per-primitive texture mapping approach and understand the contribution of individual components, we conducted a series of ablation studies. These experiments isolate different aspects of our method and compare against carefully designed baselines to provide insights into why our approach works well for reflective scenes. More experiments can be found in the supplementary material.

Table 4. Ablation study: Effect of normal mapping on average image and normal quality. We evaluate on the Shiny Blender dataset [Verbin et al. 2022].

Metric	Ref-Gaussian	+ Normal Mapping	Full Model(Ours)
PSNR ↑	34.89	35.47	35.94
SSIM ↑	0.974	0.975	0.977
LPIPS ↓	0.053	0.051	0.047
Normal MAE ↓	2.078	1.845	1.825

*Impact of Normal Mapping.* Our previous experiments suggested that normal mapping plays a particularly important role in the performance improvements observed with our method. To isolate this effect, we implemented a variant of the baseline that uses texture mapping only for normals while keeping other attributes (albedo, roughness, metallic) as per-primitive constants.

The results in Table 4 confirm that normal mapping alone accounts for a substantial portion of the performance improvement. This is particularly evident in the normal mean angular error (MAE) metric, where normal mapping significantly reduces the error compared to the baseline.

The effectiveness of normal mapping for reflective scenes can be attributed to the fact that reflective surfaces often exhibit high-frequency normal variations that are difficult to capture with a single normal per primitive and that more accurate and detailed normals lead to more precise reflection directions and therefore better specular highlights which is achieved by our spatially varying normals.

While normal mapping provides the most significant improvement, our full model with texture mapping for all material properties achieves the best overall performance, demonstrating that each component contributes to the final quality.

## 5 LIMITATIONS AND DISCUSSION

While our per-primitive texture mapping approach significantly enhances the representation power of 2D Gaussian Splatting for the reflective setting, it comes with several limitations that present opportunities for future work:

*Storage Overhead.* Storing material textures for each primitive introduces additional memory requirements. Although we save some memory by encoding tangent normals with only two components, the overall storage increases with the number of primitives and texture resolution.

*Dependency on Underlying Rendering Model.* Our method is designed to be generic and applicable to any Gaussian splatting variant with material attributes. While it enhances reconstruction quality through increased expressivity, it cannot overcome fundamental limitations of the underlying rendering model. For scenes where the physical assumptions of the model are violated (e.g., complex shadowing, grazing angle reflections, multiple level of reflections), our approach may struggle to produce accurate results. In some cases, the additional degrees of freedom provided by normal mapping can lead to overfitting to noise when the underlying model cannot



explain the observed data. This explains why we can observe more substantial improvements for simpler reflective scenes compared to more complex ones sometimes.

*Uniform Texture Resolution.* In the current implementation, we assign textures of uniform resolution to all primitives regardless of their size or importance in the scene. This approach is inefficient for large unbounded scenes where distant primitives occupy few pixels but still receive the same texture resolution as foreground elements. A more sophisticated approach would involve adaptive texture allocation based on primitive size, viewing distance, or local detail complexity. Primitives in the background could potentially use single attribute values while reserving detailed textures for foreground elements.

*Filtering Limitations.* Our implementation currently relies on bilinear filtering for texture sampling. While this works well for the scenes in our evaluation, it does not fully address texture minification artifacts that might appear in more challenging scenarios. Implementing proper mipmapping with trilinear filtering would be beneficial but challenging to integrate with the non-antialiased nature of 2D Gaussian primitives. Potential solutions could involve combining our approach with screen-space antialiasing techniques or developing specialized filtering methods for Gaussian-based representations.

Despite these limitations, our experimental results demonstrate that per-primitive texture mapping significantly improves the visual quality of reflective scenes while maintaining real-time rendering performance. The ability to capture fine normal details through normal mapping proves particularly valuable for specular reflections, where small normal variations can have substantial visual impact. Furthermore, by leveraging hardware-accelerated texture filtering through our atlas-based implementation, we achieve these quality improvements with minimal performance overhead compared to traditional Gaussian splatting approaches.

## 6 CONCLUSION

We presented a method that enhances 2D Gaussian Splatting for reflective scenes by introducing per-primitive texture mapping. By leveraging the flat nature of 2D Gaussians to define textures of material properties, our approach enables high-frequency detail representation without increasing primitive count. Our hardware-accelerated implementation using texture atlases demonstrates that classical computer graphics techniques can be effectively integrated with modern differentiable rendering approaches.

The results show that this representation significantly improves the quality of specular reflections, particularly through detailed normal mapping, while maintaining real-time performance. Our work bridges the gap between explicit primitive-based representations and high-quality material modeling, offering advantages of both approaches.

Future work could explore several promising directions like advanced filtering techniques like anisotropic filtering for improved quality at grazing angles and compressed texture formats to reduce memory requirements.

## ACKNOWLEDGMENTS

This work was granted access to the HPC resources of IDRIS under the allocation 20XX-AD010616156 made by GENCI.

## REFERENCES

- Brent Burley and Dylan Lacewell. 2008. Ptex: Per-Face Texture Mapping for Production Rendering. In *Proceedings of Eurographics Symposium on Rendering*. Eurographics Association. <https://graphics.pixar.com/library/Ptex/paper.pdf>
- Brian Chao, Hung-Yu Tseng, Lorenzo Porzi, Chen Gao, Tuotuo Li, Qibo Li, Ayush Saraf, Jia-Bin Huang, Johannes Kopf, Gordon Wetzstein, and Changil Kim. 2025. Textured Gaussians for Enhanced 3D Scene Appearance Modeling. In *Proceedings of the IEEE/CVF Conference on Computer Vision and Pattern Recognition (CVPR)*. <https://arxiv.org/abs/2411.18625>
- Anpei Chen, Zexiang Xu, Andreas Geiger, Jingyi Yu, and Hao Su. 2022. TensorRF: Tensorial Radiance Fields. In *Proceedings of the European Conference on Computer Vision (ECCV)*.
- Sara Fridovich-Keil, Giacomo Meanti, Frederik Rahbæk Warburg, Benjamin Recht, and Angjoo Kanazawa. 2023. K-Planes: Explicit Radiance Fields in Space, Time, and Appearance. In *Proceedings of the IEEE/CVF Conference on Computer Vision and Pattern Recognition (CVPR)*.
- Sara Fridovich-Keil, Alex Yu, Matthew Tancik, Qinhong Chen, Benjamin Recht, and Angjoo Kanazawa. 2022. Plenoxels: Radiance fields without neural networks. In *Proceedings of the IEEE/CVF conference on computer vision and pattern recognition*. 5501–5510.
- Jian Gao, Chun Gu, Youtian Lin, Zhihao Li, Hao Zhu, Xun Cao, Li Zhang, and Yao Yao. 2024. Relightable 3D Gaussians: Realistic Point Cloud Relighting with BRDF Decomposition and Ray Tracing. In *Proceedings of the European Conference on Computer Vision (ECCV)*. <https://arxiv.org/abs/2311.16043>
- Wenhao Ge, Tao Hu, Haoyu Zhao, Shu Liu, and Ying-Cong Chen. 2023. Ref-NeuS: Ambiguity-Reduced Neural Implicit Surface Learning for Multi-View Reconstruction with Reflection. In *Proceedings of the IEEE/CVF International Conference on Computer Vision (ICCV)*. IEEE, 4251–4260.
- Henri Gouraud. 1971. Continuous shading of curved surfaces. In *Proceedings of the 2nd conference on Computer graphics and interactive techniques*. ACM, 747–755.
- Binbin Huang, Zehao Yu, Anpei Chen, Andreas Geiger, and Shenghua Gao. 2024. 2d gaussian splatting for geometrically accurate radiance fields. In *ACM SIGGRAPH 2024 conference papers*. 1–11.
- Zhentao Huang and Minglun Gong. 2024. Textured-GS: Gaussian Splatting with Spatially Defined Color and Opacity. *arXiv preprint arXiv:2407.09733* (2024). <https://arxiv.org/abs/2407.09733>
- Yingwenqi Jiang, Jiadong Tu, Yuan Liu, Xifeng Gao, Xiaoxiao Long, Wenping Wang, and Yuxin Ma. 2024a. GaussianShader: 3D Gaussian Splatting with Shading Functions for Reflective Surfaces. In *Proceedings of the IEEE/CVF Conference on Computer Vision and Pattern Recognition (CVPR)*. IEEE, 1185–1194. <https://doi.org/10.1109/CVPR.2024.00127>
- Zijie Jiang, Tianhan Xu, and Hiroharu Kato. 2024b. Rethinking Directional Parameterization in Neural Implicit Surface Reconstruction. In *Proceedings of the European Conference on Computer Vision (ECCV)*. Springer, 127–142.
- Bernhard Kerbl, Georgios Kopanas, Thomas Leimkühler, and George Drettakis. 2023. 3d gaussian splatting for real-time radiance field rendering. *ACM Trans. Graph.* 42, 4 (2023), 139–1.
- D.P. Kingma and J.B. Ba. 2015. Adam: A Method for Stochastic Optimization. *International Conference on Learning Representations (ICLR)* (2015). <https://arxiv.org/abs/1412.6980>
- Marc Levoy. 1988. Display of Surfaces from Volume Data. *IEEE Computer Graphics and Applications* 8, 3 (1988), 29–37.
- Zhaoshuo Li, Thomas Müller, Alex Evans, Russell H Taylor, Mathias Unberath, Ming-Yu Liu, and Chen-Hsuan Lin. 2023. Neuralangelo: High-fidelity neural surface reconstruction. In *Proceedings of the IEEE/CVF Conference on Computer Vision and Pattern Recognition*. 8456–8465.
- Ruofan Liang, Huiting Chen, Chunlin Li, Fan Chen, Selvakumar Panneer, and Nandita Vijaykumar. 2023. ENVIDR: Implicit Differentiable Renderer with Neural Environment Lighting. In *Proceedings of the IEEE/CVF International Conference on Computer Vision (ICCV)*. IEEE, 79–89.
- Zhihao Liang, Qi Zhang, Ying Feng, Ying Shan, and Kui Jia. 2024. GS-IR: 3D Gaussian Splatting for Inverse Rendering. In *Proceedings of the IEEE/CVF Conference on Computer Vision and Pattern Recognition (CVPR)*. 21644–21653.
- Lingjie Liu, Jiatao Gu, Kyaw Zaw Lin, Tat-Seng Chua, and Christian Theobalt. 2020. Neural Sparse Voxel Fields. In *NeurIPS*.
- Yuan Liu, Peng Wang, Cheng Lin, Xiaoxiao Long, Jiepeng Wang, Lingjie Liu, Taku Komura, and Wenping Wang. 2023. NeRO: Neural Geometry and BRDF Reconstruction of Reflective Objects from Multiview Images. *ACM Trans. Graph.* 42, 4, Article 114 (jul 2023), 22 pages.

- Nelson Max. 1995. Optical models for direct volume rendering. *IEEE Transactions on Visualization and Computer Graphics* 1, 2 (1995), 99–108.
- Ben Mildenhall, Pratul P. Srinivasan, Matthew Tancik, Jonathan T. Barron, Ravi Ramamoorthi, and Ren Ng. 2020. NeRF: Representing Scenes as Neural Radiance Fields for View Synthesis. In *ECCV*. Springer, 405–421.
- Thomas Müller, Alex Evans, Christoph Schied, and Alexander Keller. 2022. Instant neural graphics primitives with a multiresolution hash encoding. *ACM transactions on graphics (TOG)* 41, 4 (2022), 1–15.
- Bui Tuong Phong. 1975. Illumination for computer generated pictures. *Commun. ACM* 18, 6 (1975), 311–317.
- Budirijanto Purnomo, Jonathan D Cohen, and Subodh Kumar. 2004. Seamless texture atlases. In *IEEE Visualization, 2004. VIS 2004*. IEEE, 273–280. <https://doi.org/10.1109/VISUAL.2004.91>
- Pratul P. Srinivasan, Boyang Deng, Xiuming Zhang, Matthew Tancik, Ben Mildenhall, and Jonathan T. Barron. 2021. NeRV: Neural Reflectance and Visibility Fields for Relighting and View Synthesis. In *Proceedings of the IEEE/CVF Conference on Computer Vision and Pattern Recognition (CVPR)*. 7495–7504. <https://doi.org/10.1109/CVPR46437.2021.00741>
- Cheng Sun, Jaesung Choe, Charles Loop, Wei-Chiu Ma, and Yu-Chiang Frank Wang. 2024. Sparse Voxels Rasterization: Real-time High-fidelity Radiance Field Rendering. *arXiv preprint arXiv:2412.04459* (2024).
- Jingxiang Sun, Yiming Gao, Xuan Wang, Qi Zhang, Hujun Bao, and Xiaowei Zhou. 2022. Improved Direct Voxel Grid Optimization for Radiance Fields. *arXiv:2206.05085 [cs.CV]*
- Zhe Jun Tang and Tat-Jen Cham. 2024. 3iGS: Factorised Tensorial Illumination for 3D Gaussian Splatting. In *Proceedings of the European Conference on Computer Vision (ECCV)*. Springer. [https://doi.org/10.1007/978-3-031-72630-9\\_9](https://doi.org/10.1007/978-3-031-72630-9_9)
- Dor Verbin, Peter Hedman, Ben Mildenhall, Todd Zickler, Jonathan T Barron, and Pratul P Srinivasan. 2022. Ref-nerf: Structured view-dependent appearance for neural radiance fields. In *Proceedings of the IEEE/CVF CVPR*. IEEE, 5481–5490.
- Peng Wang, Lingjie Liu, Yuan Liu, Christian Theobalt, Taku Komura, and Wenping Wang. 2021. Neus: Learning neural implicit surfaces by volume rendering for multi-view reconstruction. *arXiv preprint arXiv:2106.10689* (2021).
- Zhou Wang, Alan C Bovik, Hamid R Sheikh, and Eero P Simoncelli. 2004. Image quality assessment: from error visibility to structural similarity. *IEEE transactions on image processing* 13, 4 (2004), 600–612.
- Tong Wu, Jiaqi Wang, Xingang Pan, Xudong Xu, Christian Theobalt, Ziwei Liu, and Dahua Lin. 2022. Voxurf: Voxel-based efficient and accurate neural surface reconstruction. *arXiv preprint arXiv:2208.12697* (2022).
- Tian-Xing Xu, Wenbo Hu, Yu-Kun Lai, Ying Shan, and Song-Hai Zhang. 2024. Texture-GS: Disentangling the Geometry and Texture for 3D Gaussian Splatting Editing. In *Proceedings of the European Conference on Computer Vision (ECCV)*. Springer. <https://arxiv.org/abs/2403.10050>
- Yuxuan Yao, Zixuan Zeng, Chun Gu, Xiatian Zhu, and Li Zhang. 2025. Reflective Gaussian Splatting. In *ICLR*.
- Lior Yariv, Jiatao Gu, Yoni Kasten, and Yaron Lipman. 2021. Volume rendering of neural implicit surfaces. *Advances in Neural Information Processing Systems* 34 (2021), 4805–4815.
- Keyang Ye, Qiming Hou, and Kun Zhou. 2024. 3D Gaussian Splatting with Deferred Reflection. In *ACM SIGGRAPH Conference Proceedings*. <https://doi.org/10.1145/3641519.3657456>
- Richard Zhang, Phillip Isola, Alexei A Efros, Eli Shechtman, and Oliver Wang. 2018. The unreasonable effectiveness of deep features as a perceptual metric. In *Proceedings of the IEEE conference on computer vision and pattern recognition*. 586–595.
- Zuo-Liang Zhu, Beibei Wang, and Jian Yang. 2024. GS-ROR: 3D Gaussian Splatting for Reflective Object Relighting via SDF Priors. *arXiv preprint arXiv:2406.18544* (2024). <https://arxiv.org/abs/2406.18544>
- Matthias Zwicker, Hanspeter Pfister, Jeroen Van Baar, and Markus Gross. 2001. EWA Volume Splatting. In *Proceedings of the IEEE Conference on Visualization (VIS)*. IEEE, 29–36.
- Matthias Zwicker, Hanspeter Pfister, Jeroen Van Baar, and Markus Gross. 2002. EWA splatting. *IEEE Transactions on Visualization and Computer Graphics* 8, 3 (2002), 223–238.
- Matthias Zwicker, Jussi Rasanen, Mario Botsch, Carsten Dachsbacher, and Mark Pauly. 2004. Perspective accurate splatting. In *Proceedings-Graphics Interface*. 247–254.

## 7 ADDITIONAL ABLATION STUDIES

**Texture Mapping vs. Increased Primitive Count.** A natural question when evaluating our texture-based method is whether similar quality improvements could be achieved by simply increasing the number of primitives in the baseline method. To investigate this, we compared our approach against baseline models with increased primitive counts. We created versions of the baseline with  $2\times$  and  $4\times$

Table 5. Ablation study: Effect of increasing primitive count for the baseline method on average image quality. We evaluate on the Shiny Blender dataset [Verbin et al. 2022].

Metric	Ours	Ref-Gaussian	$\times 2$ Primitives	$\times 4$ Primitives
PSNR $\uparrow$	35.94	34.89	33.63	34.12
SSIM $\uparrow$	0.977	0.974	0.967	0.970
LPIPS $\downarrow$	0.047	0.053	0.061	0.057

the original number of primitives by lowering the gradient threshold for densification and increasing the frequency of cloning and splitting operations during optimization. We compare against our method that maintain the original primitive count with the  $4\times 4$  textures per primitive. Notably, even with these textures, our method has lower storage requirements than the  $2\times$  primitive count baseline. As shown in Table 5, the performance of the baseline method actually degrades as the number of primitives increases beyond the optimal point. This counter-intuitive result can be explained by the fact that increasing the number of primitives creates a more complex optimization and that more primitives require more extensive sorting operations during rendering, which can lead to primitives being placed in suboptimal orders, especially with the use of global sorting [Kerbl et al. 2023]. Primitives can also become cluttered, particularly in areas with complex geometry, leading to degraded normal estimation quality which is critical for reflective scenes.

Our texture-based approach avoids these issues by increasing representational power without increasing the number of primitives, leading to better rendering quality particularly for reflective surfaces.

**Performance with Reduced Primitive Count.** To further demonstrate the efficiency of our texture-based representation, we conducted experiments with reduced primitive counts. We created models using only 50% of the primitives used in our standard optimization process, for both the baseline method and our texture-based approach.

As illustrated in Figure 8, the baseline method with reduced primitive count suffers from significant degradation in normal reconstruction quality, exhibiting holes and artifacts due to the limited capacity of the model. In contrast, our texture-based method maintains smooth normal reconstruction even with the reduced primitive count, demonstrating the expressiveness of per-primitive texture mapping.

This experiment highlights a key advantage of our approach: it can achieve high-quality results with fewer primitives, making it particularly suitable for applications with strict performance requirements or memory constraints.

**Performance on non-specular scenes.** In Table 6, we show the performance of our method against different methods in non-specular scenes from the NeRF Synthetic dataset. Our method is capable of enhancing the baseline method thanks to the expressivity of material and normal texture splatting. It can even reach the level of performance of the vanilla 3DGS [Kerbl et al. 2023] on these scenes.

Table 6. Per-scene image quality comparison for novel view synthesis on NeRF Synthetic dataset.

	chair	drums	ficus	hotdog	lego	materials	ship
<b>PSNR <math>\uparrow</math></b>							
3DGS	35.03	26.04	35.29	37.57	33.71	30.04	31.43
3DGS-DR	32.10	25.31	28.03	35.58	32.94	28.35	29.07
Ref-Gaussian	33.73	26.25	35.50	37.19	32.58	30.72	30.44
<b>Ours</b>	34.40	26.39	35.93	37.47	33.47	31.30	30.58
<b>SSIM <math>\uparrow</math></b>							
3DGS	0.987	0.954	0.987	0.985	0.975	0.959	0.906
3DGS-DR	0.977	0.946	0.963	0.982	0.978	0.950	0.894
Ref-Gaussian	0.979	0.952	0.987	0.982	0.972	0.966	0.895
<b>Ours</b>	0.981	0.953	0.989	0.983	0.974	0.970	0.896
<b>LPIPS <math>\downarrow</math></b>							
3DGS	0.012	0.040	0.012	0.021	0.027	0.040	0.111
3DGS-DR	0.024	0.055	0.055	0.033	0.026	0.044	0.129
Ref-Gaussian	0.023	0.043	0.013	0.029	0.031	0.036	0.127
<b>Ours</b>	0.021	0.041	0.011	0.027	0.027	0.031	0.123

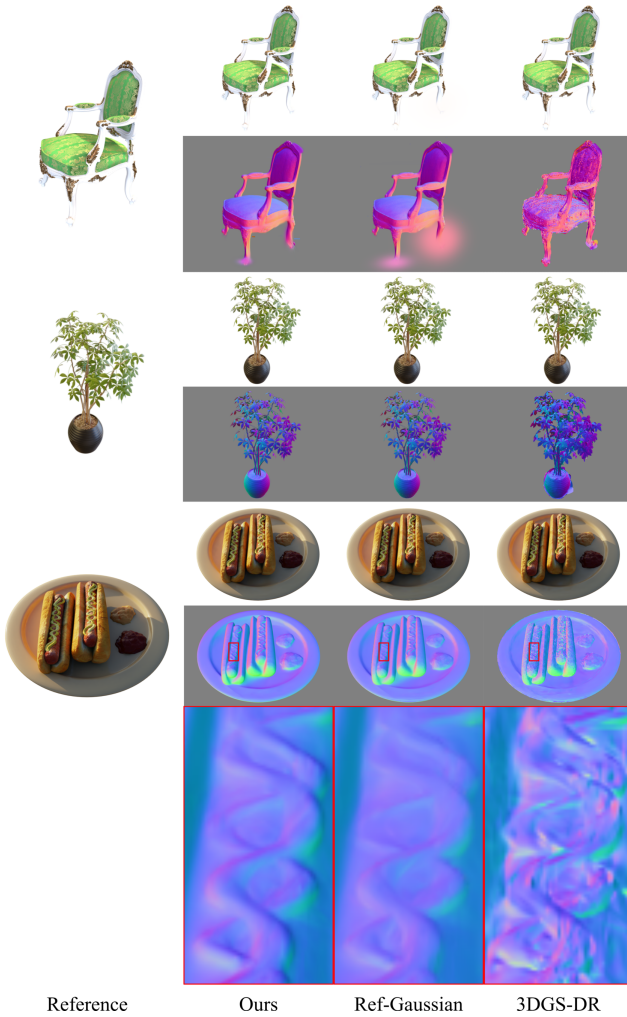


Fig. 9. Qualitative comparisons on the Synthetic NeRF dataset. From top to bottom: drums, ficus and hotdog.



Fig. 8. Comparison of novel view synthesis and normal rendering with fewer primitives

We also show in Figure 9 comparison against other reflection gaussian splatting methods where the normals produced by our method are more defined and are less noisy in comparison.